*Article*

# Investigation of EM Backscattering from Slick-Free and Slick-Covered Sea Surfaces Using the SSA-2 and SAR Images

**Honglei Zheng** [1], **Yanmin Zhang** [1,*], **Ali Khenchaf** [2], **Yunhua Wang** [1], **Helmi Ghanmi** [2] and **Chaofang Zhao** [1]

[1] College of Information Science and Engineering, Ocean University of China, 238 Songling Road, Qingdao 266100, China; zhenghonglei@stu.ouc.edu.cn or hongleizheng@hotmail.com (H.Z.); yunhuawang@ouc.edu.cn (Y.W.); zhaocf@ouc.edu.cn (C.Z.)

[2] Lab-STICC, UMR CNRS 6285, ENSTA Bretagne, 2 rue Francois Verny 29806 Brest CEDEX 9, France; ali.khenchaf@ensta-bretagne.fr (A.K.); helmi.ghanmi@ensta-bretagne.org (H.G.)

[*] Correspondence: yanminzhang@ouc.edu.cn

**Abstract:** This paper is devoted to investigating the electromagnetic (EM) backscattering from slick-free and slick-covered sea surfaces at various bands (L-band, C-band, X-band, and Ku-band) by using the second-order small slope approximation (SSA-2) and the measured synthetic aperture radar (SAR) data. It is known that the impact of slick on sea surface is mainly caused by two factors: the Marangoni damping effect and the reduction of friction velocity. In this work, the influences induced by these two factors on the sea curvature spectrum, the root mean square (RMS) height, the RMS slope, and the autocorrelation function of sea surfaces are studied in detail. Then, the slick-free and slick-covered sea surface profiles are simulated using the Elfouhaily spectrum and the Monte-Carlo model. The SSA-2 with the tapered incident wave is employed to simulate the normalized radar cross-sections (NRCSs) of sea surfaces. Furthermore, for slick-free sea surfaces, the NRCSs simulated with the SSA-2 at various bands are compared with those obtained by the first-order small slope approximation (SSA-1), the classic two-scale model (TSM), and the geophysical model functions (GMFs) at various bands, respectively. For slick-covered sea surfaces, the SSA-2-simulated NRCSs are compared with those obtained from C-band Radarsat-2 images and L-band uninhabited aerial vehicle synthetic aperture radar (UAVSAR) images, respectively. The numerical simulations illustrate that the SSA-2 can be used to study the EM backscattering from slick-free and slick-covered sea surfaces, and it has more advantages than the SSA-1 and the TSM. The works presented in this paper are helpful for understanding the EM scattering from the sea surface covered with slick, in theory.

**Keywords:** ocean remote sensing; EM scattering; sea surface; SAR; SSA-2; GMF; NRCS

## 1. Introduction

Oil spill pollution on the sea surface is harmful to marine ecosystems, fisheries, wildlife, and other societal interests. Scientists and researchers have made a great effort to monitor oil spills on the sea surface. Many scientific papers covering a wide range of topics have written about the used means of monitoring of oil spills, e.g., Salberg et al. [1], Skunes et al. [2], Lupidi et al. [3], etc. It is well-known that the synthetic aperture radar (SAR) is almost independent of atmospheric conditions, and can provide high-resolution measurements at both day and night [4]. It has been proven that SAR is a useful tool for ocean remote sensing, especially for oil spill detection and monitoring. In previous literature, the problem of oil spill monitoring has been studied mainly from two aspects. The first one focuses

on detecting oil spills by using measured SAR images [5–11]. The second one focuses on analyzing electromagnetic (EM) field scattered from clean and polluted sea surfaces [12–15]. Unlike previous papers, the motivation of this work is to investigate the influences caused by slicks on sea surface characteristics and the EM scattering from slick-covered and slick-free sea surfaces, both theoretically as well as experimentally.

The influences caused by slicks can mainly be described by two effects: the damping of small-scale sea waves, and the reduction of friction velocity. On one hand, due to the damping effects for short-gravity and capillary waves, the sea surface profile of the slick-covered sea surface is quite different from that of the slick-free surface. The damping effect is usually described by the Marangoni theory [16]. On the other hand, as a slick-covered surface is smoother, the friction velocity is reduced, and the energy transferred from the wind to sea waves is also reduced. These two effects will both directly influence the sea height spectrum.

For the EM scattering from sea surface, the backscattered field depends on the sea roughness state. In the past decades, various approximate methods have been developed for the estimation of the EM scattering field from rough sea surface. Among these methods, the Kirchhoff approximation (KA) [17], the small perturbation method (SPM) [18], and the two-scale model (TSM) are effective methods for estimating the scattering coefficient. Unfortunately, all these three methods are only available in certain conditions or involve a cutoff parameter to separate sea waves into small and large scales. The small slope approximation (SSA) is a unified model that is suitable for large-scale, intermediate-scale, and small-scale roughness surfaces under the condition that the tangent of grazing angles of incident/scattered waves sufficiently exceeds the root mean square (RMS) slope [19,20]. According to the requirement of accuracy, the SSA can be divided into the first-order SSA (SSA-1) and the second order SSA (SSA-2). The SSA-1 involves less computation, but it cannot provide cross-polarized (HV or VH) scattering coefficient estimation in backscatter configurations. In contrast, the SSA-2 does not involve any arbitrary parameters and it could provide predictions for cross-polarized scattering coefficient estimation. To our knowledge, the SSA-2 has never been used to study the EM scattering from both slick-free and slick-covered sea surfaces. The main contribution of this work is to study EM scattering from sea surfaces covered with and without slick, both theoretically and experimentally.

This paper is organized as follows: the theoretical derivations of the damping model and the SSA-2 are briefly reviewed in Section 2. Numerical simulations of normalized radar cross-sections (NRCSs) of slick-free and slick-covered sea surfaces are presented and discussed in Section 3. Finally, conclusions and perspective are drawn in Section 4.

## 2. Theory and Methodology

### 2.1. The Damping Model

The influences of the slick can mainly induce by two effects, i.e., the damping effect for small-scale sea waves, and the reduction of friction velocity. In general, the damping effect caused by slick is modeled by the Marangoni theory [13,21]. The damping ratio induced by slick can be expressed as:

$$y_r(k_w) = \frac{1 \pm 2\tau + 2\tau^2 - X + Y(X + \tau)}{1 \pm 2\tau + 2\tau^2 - 2X + 2X^2}, \tag{1}$$

where $\tau$, $X$, and $Y$ are given as:

$$\tau = \sqrt{\frac{\omega_D}{2\omega}}, X = \frac{E_0 k_w^2}{\rho(2\nu\omega^3)^{1/2}}, Y = \frac{E_0 k_w}{4\nu\rho\omega}. \tag{2}$$

In Equation (1), $k_w$ is the wavenumber of sea waves, $\omega$ is the angular frequency of sea waves, $\nu$ is dynamic viscosity, and $\rho$ is the density of seawater, respectively. $E_0$ denotes the elasticity modulus, and $\omega_D$ is a characteristic pulsation. In this work, we investigate two kinds of slicks, which are denoted as

slick-a ($E_0$ = 9 mN/s, $\omega_D$ = 6 rad/s) and slick-b ($E_0$ = 25 mN/s, $\omega_D$ = 11 rad/s), and correspond to organic films measured in two cases. These values were retrieved from field experiments, and have been used in previous works for studying the impacts of slicks on EM scattering field from sea surface [12,13]. It should be noted that this model does not involve the thickness of slick.

Besides, given that the slick film may be partially dispersed by the winds and the sea waves, a fractional filling factor *F* is introduced to modify the damping ratio. Finally, the damping ratio can be written as [13]:

$$y(k_w) = \frac{1}{1 - F + F/y_r(k_w)}. \tag{3}$$

Obviously, the damping model is homogeneous, which implies that the damping effect is not associated with wind direction.

As the small-scale waves of the slick-covered surface are damped, the roughness of the surface is reduced. As a consequence, the energy transferred from the wind to sea waves, which is related to the friction velocity, is reduced. This phenomenon has been observed in field experiments: the friction velocity of the slick-covered surface is smaller than the slick-free surface. The friction velocity of a slick-covered surface $u_{*c}$ can be calculated empirically with [22]:

$$u_{*c} = \beta u_*, \tag{4}$$

where $\beta < 1$. In this work, the value of $\beta$ suggested by Gade et al. is adopted [23]; i.e., $\beta$ = 0.7. Thus, the spectrum of sea surface covered by slick is related to the clean sea surface spectrum by:

$$S_s(k_w, u_{*c}) = \frac{S_w(k_w, u_{*c})}{y(k_w)}, \tag{5}$$

where $S_s(k_w, u_{*c})$ denotes the spectrum covered by slick, and $S_w(k_w, u_{*c})$ denotes the clean sea surface spectrum.

*2.2. The Second-Order Small Slope Approximation (SSA-2)*

According to the theory of small slope approximation, the scattering amplitude of the second order can be written as [19,20]:

$$\mathbf{S}(\mathbf{k}^e, \mathbf{k}_0^e) = \frac{2\sqrt{q_0 q}}{(q_0 + q)\sqrt{P_{inc}}} \int \frac{d\mathbf{r}}{(2\pi)^2} G(r, h) \exp\left[-j(\mathbf{k}^e - \mathbf{k}_0^e) \cdot \mathbf{r} + j(q_0 + q)h(\mathbf{r})\right] \\ \times \left[B(\mathbf{k}^e, \mathbf{k}_0^e) - \frac{j}{4} \int M(\mathbf{k}^e, \mathbf{k}_0^e; \xi) h(\xi) \exp(j\xi \cdot \mathbf{r}) d\xi\right] \tag{6}$$

The incoherent scattering amplitude can be calculated with $\Delta\mathbf{S}(\mathbf{k}^e, \mathbf{k}_0^e) = \mathbf{S}(\mathbf{k}^e, \mathbf{k}_0^e) - \langle\mathbf{S}(\mathbf{k}^e, \mathbf{k}_0^e)\rangle$. The incoherent scattering coefficient can be calculated with the incoherent scattering amplitude by:

$$\sigma_0 = 16\pi^3 q_0 q \Delta\mathbf{S}(\mathbf{k}^e, \mathbf{k}_0^e)[\Delta\mathbf{S}(\mathbf{k}^e, \mathbf{k}_0^e)]^*. \tag{7}$$

The meanings of the parameters in the equations above can be found in the Appendix A. As shown in Equation (6), the calculation of scattering amplitude of the SSA-2 is rather complex, as it requires the calculation of a fourfold integral. This involves a large amount of computation, and it takes a long time to perform the numerical simulation, which is the main drawback of the SSA-2. For more details about the numerical simulations mentioned above, please refer to Appendix A.

Additionally, to model the seawater dielectric constant, the Debye model is employed in all simulations, where the temperature equals 20 °C, and the salinity equals 35 ppt. For microwave scattering, the dielectric constant of the oil is much smaller than seawater; the oil layer can be regarded as a "transparent" layer. That is to say, the EM scattering energy is mainly contributed by the seawater under oil. Besides, the thickness of a surface film (either a monomolecular slick or a thin oil spill)

is small compared with the penetration depth of microwaves into the water. Thus, in numerical simulation, the impact induced by the dielectric constant of slick has been neglected [23].

## 3. Numerical Simulations and Discussions

### 3.1. Impacts of Slick on the Sea Surface

The EM scattering field is highly dependent on the characteristics of the rough surface. To study the EM scattering from the slick-covered sea surface, it is necessary to make how the slick influences the sea surface clear. Therefore, in this part, the impacts of slicks on a clean sea surface are simulated and discussed from several aspects, including the sea curvature spectrum, the RMS height, RMS slope, and the autocorrelation function.

3.1.1. The Damping Ratio for Various Bands

According to Section 2, the damping ratio can be calculated with Equation (3). Figure 1 displays the damping ratios of two kinds of slicks.
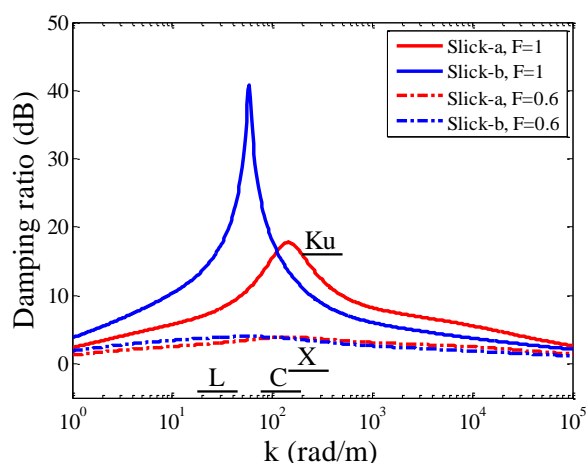


**Figure 1.** The damping ratios of different slicks and fractional filling factors (*F*).

In Figure 1, it is observed that the damping ratios first increase, and then decrease with sea wavenumber. There exist peak values for both kinds of slicks. For about $k$ <100 rad/m, slick-b has a larger damping ratio, while for about $k$ >100 rad/m, slick-a has a larger damping ratio. The damping effect becomes more significant with a larger fractional filling parameter $F$. According to Bragg scattering theory, the Bragg wavenumber of sea surface can be written as:

$$k_B = 2k^e \sin\theta_i, \tag{8}$$

where $k^e$ is the electromagnetic wavenumber, and $\theta_i$ is the incident angle.

Figure 2 shows the Bragg wavenumber ranges corresponding to L-band, C-band, X-band, and Ku-band electromagnetic waves, respectively. The damping ratios that correspond to $F$ = 1 and $F$ = 0.6 of two kinds of slicks for four bands are plotted as functions of the incident angles in Figure 2. In Figure 2a,c, it can be noted that the damping ratios for the X-band and Ku-band monotonically decrease with incident angle. While for the C-band, the damping ratio first increases and then decreases. For the L-band, the damping ratio monotonically increases with incident angle. In Figure 2b,d, it can be noted that the damping ratios for the C-band, X-band, and Ku-band decrease with incident angle. While for the L-band, the damping ratio increases with incident angle. The C-band has a larger damping ratio than the other three bands. Comparing Figure 2a with Figure 2c, and Figure 2b with Figure 2d, $F$ makes significant influences on the damping ratios at four bands, which correspond to Figure 1. According to equations (3) and (8), we know that the Bragg wavenumbers that correspond

to different bands are different, and the damping ratios for different Bragg wavenumbers are also different. As a consequence, the damping effects caused by slicks on the L-band, C-band, X-band, and Ku-band are different.
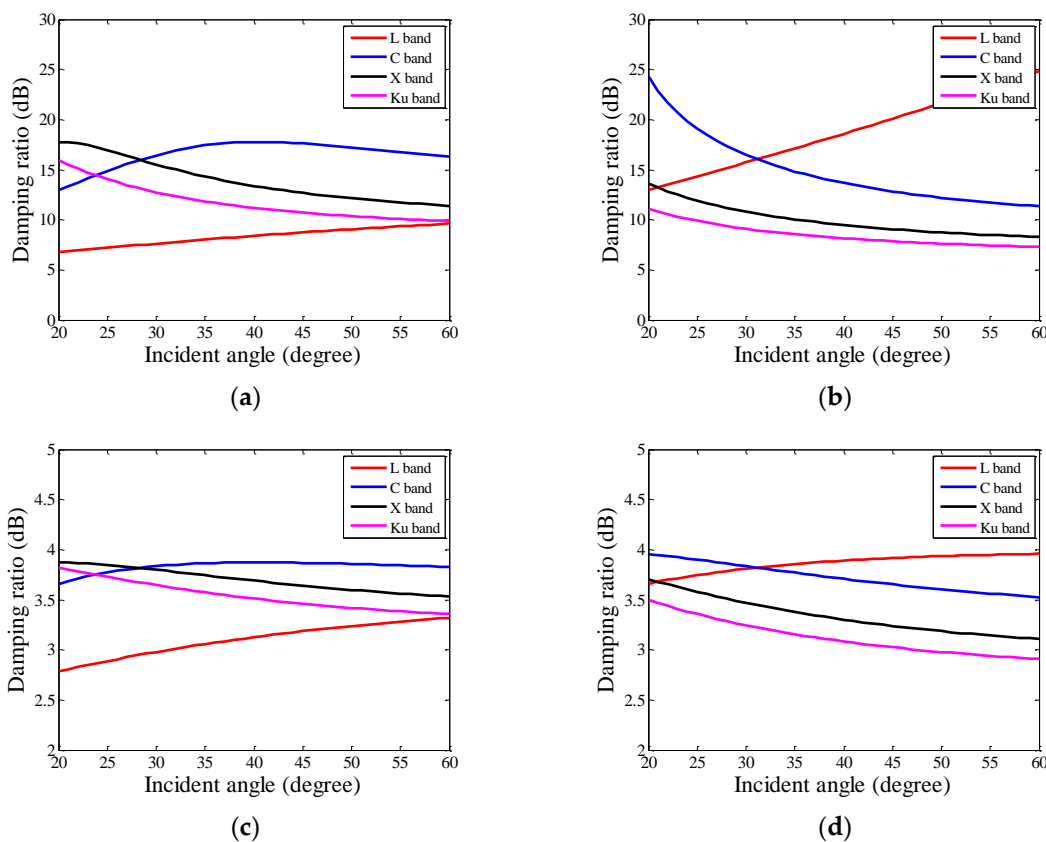


**Figure 2.** The damping ratios in relation with the incident angle. (**a**) Slick-a, *F* = 1. (**b**) Slick-b, *F* = 1. (**c**) Slick-a, *F* = 0.6. (**d**) Slick-b, *F* = 0.6.

3.1.2. Impacts of Slick on the Curvature Spectrum

A sea spectrum describes the distribution of each harmonic component of the sea surface as functions of the spatial wavenumber and wind direction. Usually, it can be expressed as:

$$S(k_w, \varphi) = S_0(k_w) \cdot f(k_w, \varphi), \tag{9}$$

where $S_0(k_w)$ represents the omnidirectional part and $f(k_w, \varphi)$ represents the spreading function. $\varphi$ is the angle between the observation angle and upwind direction. In the literature, various sea spectral models have been proposed; among these models, the Elfouhaily spectrum is one of the most widely used sea spectra in ocean remote sensing [24,25]. In this work, the Elfouhaily spectrum is employed to describe sea waves.

Figure 3 shows the impacts of the Marangoni damping effect (denoted as D), the reduction of friction velocity (denoted as R), and *F* on the curvature spectrum $B(k_w)$, where $B(k_w) = k_w^3 S(k_w)$, and $S(k_w) = \int_{-\pi}^{\pi} S(k_w, \varphi) d\varphi$. The wind speed at 10-m height ($U_{10}$) is set as 7 m/s. In Figure 3a, we can note that the short-gravity and capillary waves are damped significantly due to the Marangoni effect. In fact, the Marangoni effect mainly influences the small-scale waves, and it makes no influences on the large-scale waves. Moreover, slick-b has a heavier damping effect than slick-a when *k* <100 rad/m, while slick-a has a heavier damping effect when *k* >100 rad/m. Besides, the reduction of friction velocity mainly influences the large-scale waves and makes slight influences on the small-scale waves. The reduction of friction velocity is not associated with the properties of slicks. As illustrated

in Figure 3b, the fractional filling factor $F$ only influences the short-gravity and capillary waves. The differences between the two kinds of slicks become smaller when the value of $F$ gets smaller.
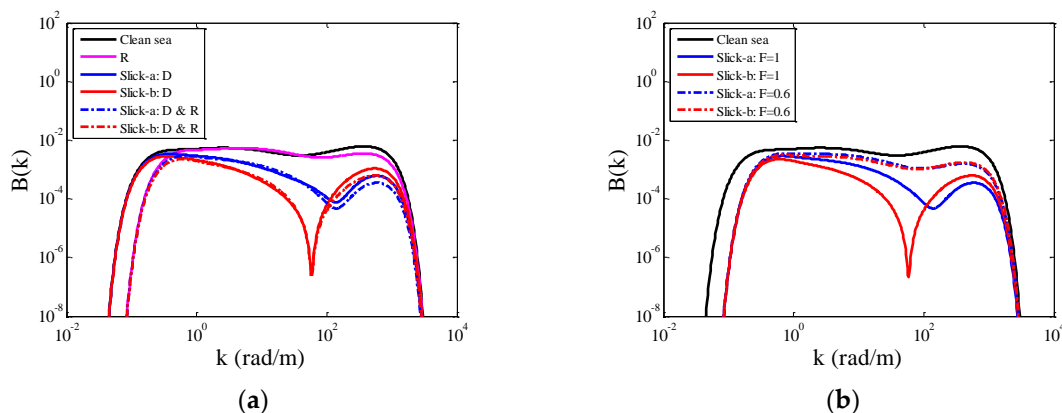


**Figure 3.** The curvature spectra, $U_{10} = 7$ m/s. (**a**) Influenced by the Marangoni effect and reduction of friction velocity, $F = 1$. (**b**) Influenced by $F$ with D and R.

### 3.1.3. Impacts of Slick on the RMS Height and the RMS Slope

The profile of the sea spectrum changes when an oil slick presents on the sea surface, which results in changes in the slope variances and height variances. Figure 4 presents the RMS heights of the sea surfaces under different conditions. It can be observed in Figure 4 that the influences of the Marangoni effect and $F$ on the RMS height are quite small. In addition, the curves of the two kinds of slicks are similar, and the reduction of friction velocity is the main reason for the reduction of the RMS height.
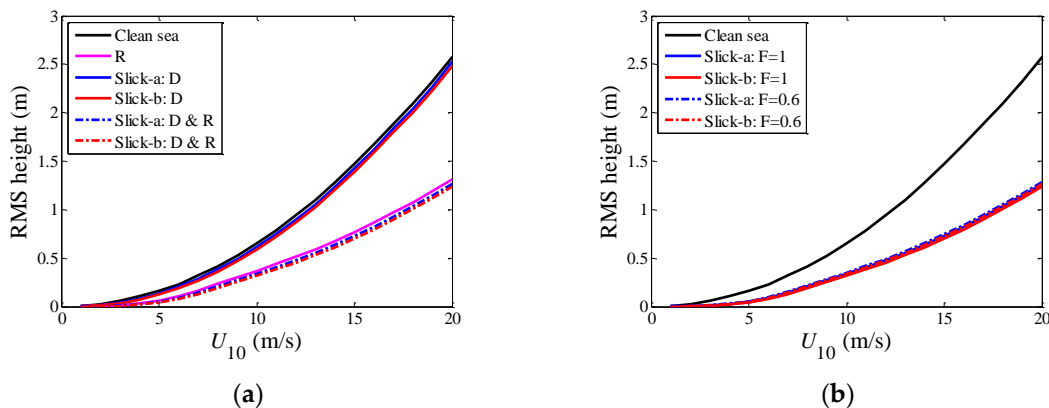


**Figure 4.** The RMS heights, $U_{10} = 7$ m/s. (**a**) Influenced by the Marangoni effect and the reduction of friction velocity, $F = 1$. (**b**) Influenced by $F$ with D and R.

Figure 5 shows the RMS slopes of sea surfaces plotted as functions of wind speed. In fact, the RMS height mainly depends on the large-scale waves, while the RMS slope depends both on the large-scale and the small-scale waves. Thus, unlike the RMS height, the influence of the reduction of the friction velocity on the RMS slope cannot be neglected. The influence caused by the Marangoni effect seems more obvious than the reduction of friction velocity. For Figure 5b, the value of $F$ has a significant influence on the RMS slope. The RMS slope is also modulated by the physical property of different kinds of slicks.
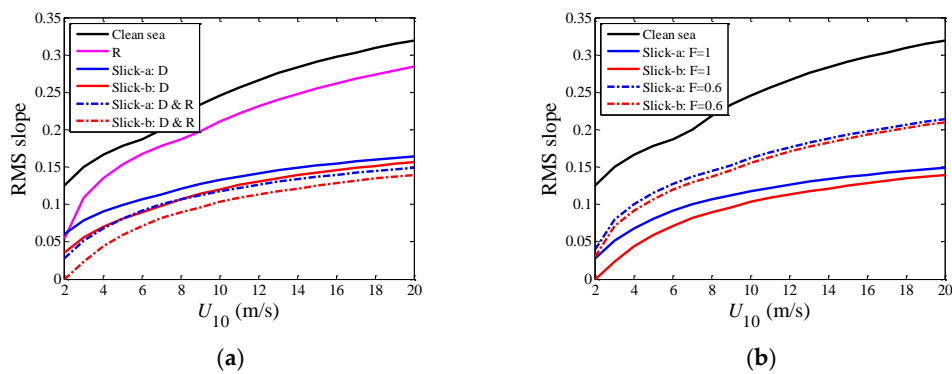
**Figure 5.** The root mean square (RMS) slopes of sea surfaces, $U_{10}$ = 7 m/s. (**a**) Influenced by the Marangoni effect and reduction of friction velocity. (**b**) Influenced by $F$ with D and R.

### 3.1.4. Impacts of Slick on the Autocorrelation Function

The autocorrelation of the displacement field of the sea surface profile corresponds to the inverse Fourier transform of the sea spectrum. It describes the correlations between two arbitrary points on the rough surface. In the numerical simulation by the SSA-2, the scattering coefficient is related to the autocorrelation function. As limited by the length of the paper, we cannot provide a detailed discussion here; for more discussions about the autocorrelation function, please refer to Voronovich et al. [20]. It is interesting to compare the autocorrelation functions of slick-free and slick-covered sea surfaces, since the correlation length and the autocorrelation function shape are also closely related to the roughness of the rough surface.

Figure 6 shows the autocorrelation functions normalized by the height variances of the sea surfaces. In Figure 6a, the impacts of slicks on the autocorrelation function are similar to the RMS height. The reduction of friction velocity is very influential upon the autocorrelation function. In contrast, the Marangoni effect changes the autocorrelation function slightly. In Figure 6b, the value of $F$ also makes negligible influences on the autocorrelation function. Through Figure 6, it can be noted that the reduction of friction speed makes a shorter correlation length, and the two kinds of slicks produce similar impacts on the shape of autocorrelation functions.
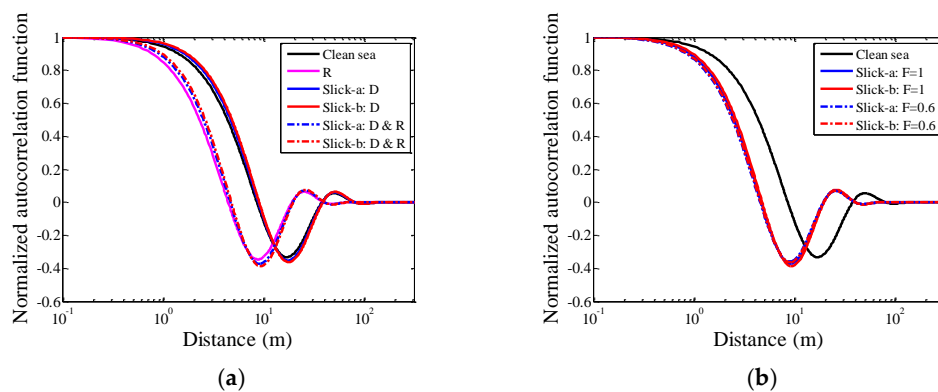


**Figure 6.** The autocorrelation functions, $U_{10}$ = 7 m/s. (**a**) Influenced by the Marangoni effect and reduction of friction velocity. (**b**) Influenced by $F$ with D and R.

### 3.2. NRCS of Slick-Free and Slick-Covered Sea Surfaces

In this part, the normalized radar cross-sections (NRCS) of slick-free and slick-covered sea surfaces are estimated according to Section 2. For slick-free sea surface, the NRCSs simulated by the SSA-2 are compared with those obtained using the geophysical model functions (GMFs), the classic TSM, and the SSA-1, respectively. For slick-covered sea surface, the simulated NRCSs of the SSA-2 are

compared with the SAR data acquired by the C-band Radarsat-2 and the L-band uninhabited aerial vehicle synthetic aperture radar (UAVSAR).

### 3.2.1. NRCS of Slick-Free Sea Surfaces

GMFs are empirical models that are related to the incident angle, wind speed, and wind direction. The GMFs are often applied for wind field retrieval. It has been proven that GMFs could provide accurate predictions in practical applications. Thus, the NRCS estimated with GMFs can be regarded as reliable references. To evaluate the effectiveness of the SSA-2 for sea surface NRCSs estimation, in this part, the NRCSs calculated with the SSA-2 are compared with those obtained from L-band GMF [26], C-band CMOD7 [27], C-band CSARMOD [28], X-band XMOD2 [29], and Ku-band NSCAT4 [30], respectively. Besides, the SSA-2 is also compared with the classic TSM and the SSA-1.

Figure 7 shows the NRCSs computed using the SSA-1, the SSA-2, the TSM, and the GMFs. It should be noted that the L-band GMF can be employed only for HH polarization, the CMOD7 is valid for VV polarization, the CSARMOD is valid for both HH and VV polarizations, the XMOD2 is valid for VV polarization, and the NSCAT4 is valid for both HH and VV polarizations (where 'V' denotes the vertical polarization, and 'H' denotes the horizontal polarization). Firstly, in Figure 7, it can be noted that the difference between the SSA-1 and the SSA-2 is quite small both for HH and VV polarization. Compared with TSM, it is quite similar for incident angles larger than 30° for all four bands. While the incident angle is smaller than 30°, there exist larger differences among the C-band, X-band, and Ku-band. With respect to the SSA-2, the scattering coefficient is influenced by surface sample intervals and surface length. The discrepancies between the SSA-2 and TSM for incident angles smaller than 30° at the C-band, X-band, and Ku-band may be introduced by the surface length. For an HV-polarized channel, the curves of the SSA-2 and the TSM are similar to each other. Through Figure 7a–d, compared with GMFs at different bands, the VV polarized scattering coefficient with the SSA-2 agrees well with the GMFs. While for HH-polarized channels at the C-band and Ku-band, there exist quite larger differences between the SSA-2 and the NSCAT4. That is to say, the SSA-2 simulates VV-polarized NRCS more accurately than HH polarization.
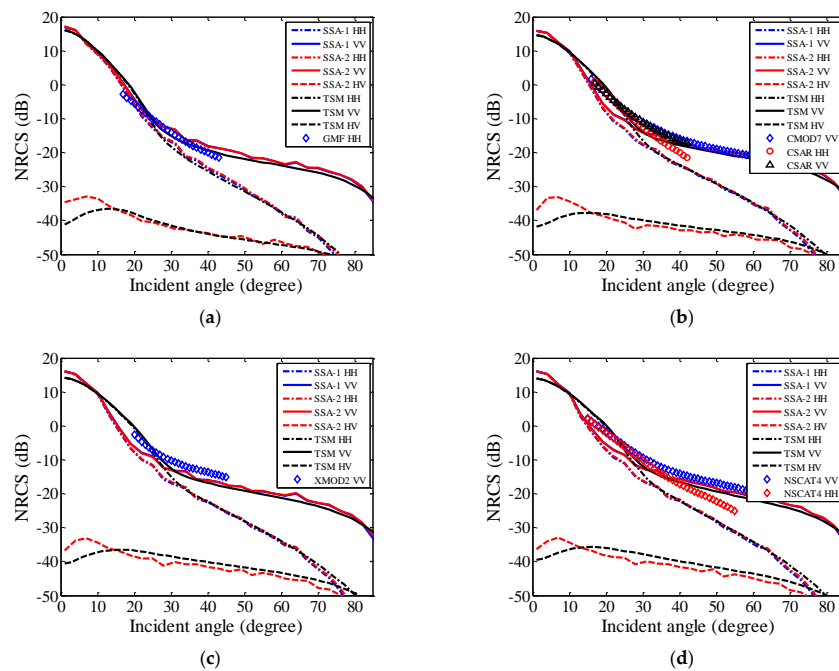


**Figure 7.** The second-order small slope approximation (SSA-2) compared with other models, including the first-order small slope approximation (SSA-1), two-scale model (TSM), and geophysical model functions (GMFs). In relation to the incident angle, $U_{10}$ = 7 m/s. (**a**) L-band, (**b**) C-band, (**c**) X-band, and (**d**) Ku-band.

Figure 8 illustrates the NRCSs estimated with different methods under different wind speeds. In Figure 8, we can note that the NRCSs of the SSA-1 are almost the same with the SSA-2. Combing the results presented in Figure 7, we can know that the NRCS estimated by the SSA-1 is precise enough in most cases. However, the drawback of the SSA-1 is that it cannot provide the estimation of cross-polarized NRCS in a backscattered direction. In Figure 8a, for the SSA-2 and the TSM, it is hard to say which method is better. These two methods have similar accuracies, with small overestimation or underestimation of the NRCSs for the small or large wind speed. In Figure 8b–d, for VV-polarized NRCS estimation, the SSA-2 seems better than the TSM. In fact, the differences between the SSA-2 and the TSM are not large. That is to say, the TSM is also an effective method in EM scattering computations. Meanwhile, the main disadvantage of the TSM is that it involves an arbitrary parameter, i.e., the scale-dividing parameter ($k_d$, in this paper, $k_d = k_i/3$) separating the small- and large-scale components of the roughness. With respect to HH-polarized channels at the C-band and Ku-band, the curves of the SSA-2 are quite different from those of the GMFs. Assuming that the GMFs are precise enough, through the comparisons presented in Figure 8, we can know that the SSA-2 provides better results for a VV-polarized channel than an HH-polarized channel. The SSA-2 performs better than TSM at the C-band, X-band, and Ku-band.
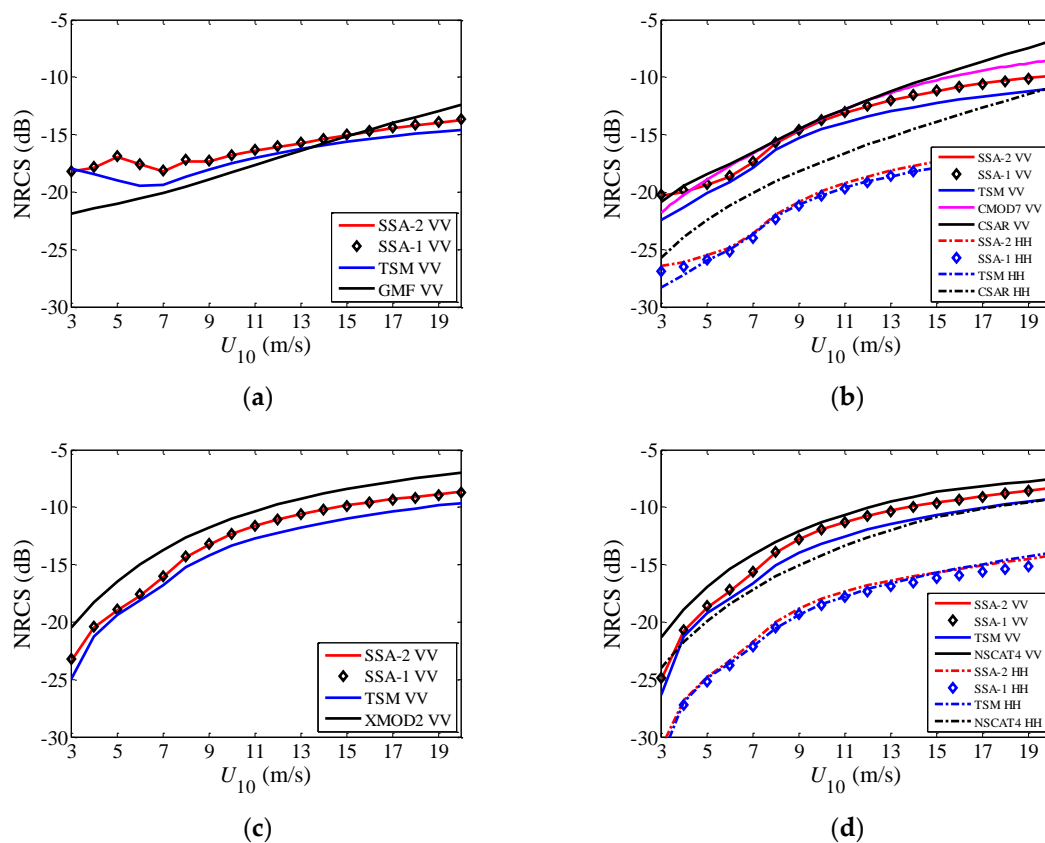


**Figure 8.** The SSA-2 compared with other models (SSA-1, TSM, and GMFs). In relation with wind speed, $\theta_i = 40°$. (**a**) L-band, (**b**) C-band, (**c**) X-band, and (**d**) Ku-band.

### 3.2.2. NRCS of Slick-Covered Sea Surfaces at the C-Band

The RADARSAT-2 data acquired at the C-band has been employed to study oil spill on sea surfaces [31]. The radarsat-2 data used in this part was acquired during the oil spill experiment conducted by the Norway Clean Seas Association for Operating Companies (NOFO) in the North Sea [32]. The acquisition time is 17:27 (UTC), 8 June 2011. The resolution in the range and azimuth directions are 5.2 m and 7.6 m, respectively. The incident angle is about 34.5~36.1°. The dark area in Figure 9 is biogenetical slick. The wind speed is 1.6~3.3 m/s.
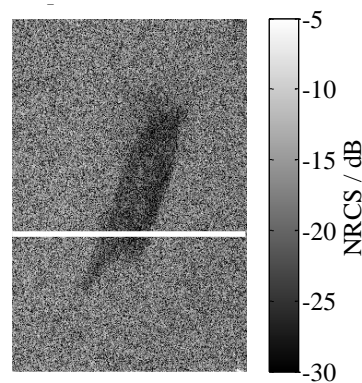
**Figure 9.** The RADARSAT-2 image related with slick.

In Figure 10, the NRCSs in VV, HH, and HV-polarized channels are presented, respectively. In the numerical simulation, the wind speed $U_{10}$ is set as 3.3 m/s. The NRCSs of RADARSAT-2 data are extracted along the white line in Figure 9. As shown in Figure 10, for clean sea surface, the VV-polarized and HH-polarized NRCSs of the SSA-2 agree better with the RADARSAT-2 data than HV-polarized channel. For the slick-covered surface, the VV-polarized NRCS estimated with the SSA-2 is consistent with the RADARSAT-2 data when $F = 0.7$.
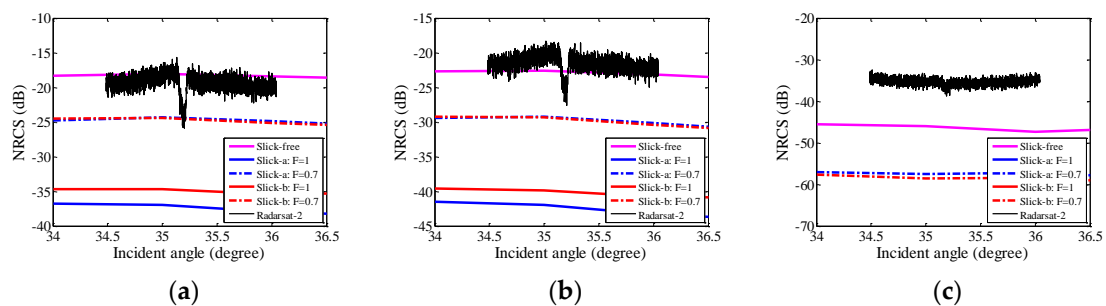


**Figure 10.** Comparison between simulated results with RADARSAT-2. (**a**) VV polarization. (**b**) HH polarization. (**c**) HV polarization.

It is well-known that the VV polarization channel is preferred because of its larger radar cross-section from the sea surface, which yields larger differences between the sea surfaces covered with and without oil slicks [33]. Combining the results exhibited in Figure 10, we can note that the VV-polarized NRCS with the SSA-2 is more suitable to study the EM scattering than the HH and HV-polarizations.

### 3.2.3. NRCS of Slick-Covered Sea Surfaces at the L-Band

The L-band SAR images used in this part are acquired by uninhabited aerial vehicle synthetic aperture radar (UAVSAR) during the Deepwater Horizon (DWH) oil spill accident in the Gulf of Mexico in 2010 [34,35]. UAVSAR is a fully polarimetric L-band SAR. The center frequency of the incident wave is 1.2575 GHz. Two multi-look (three and 12 looks in the range and azimuth directions, respectively) UAVSAR images with a 5-m slant range resolution and 7.2-m azimuth resolution are employed in this part. The SAR images used in this work were acquired from two adjacent, overlapping flight tracks that covered the main oil spills in the Gulf of Mexico. The two flight lines are gulfco_14010_10054_100_100623 (hereafter denoted as Case (a)) and gulfco_32010_10054_101_100623 (hereafter denoted as Case (b)), respectively. More information about the data are summarized in Table 1 [33].

**Table 1.** Uninhabited aerial vehicle synthetic aperture radar (UAVSAR) data information.

| Case | Data ID | Time of Acquisition | Incident Angle (°) | Wind Speed $U_{10}$ (m/s) | Wind Direction (°) |
|------|---------|---------------------|--------------------|---------------------------|--------------------|
| (a) | 14010 | 20:42 UTC 23 June 2010 | 22–65 | 2.5–5 | 115–126 |
| (b) | 32010 | 21:08 UTC 23 June 2010 | 22–65 | 2.5–5 | 115–126 |

The UAVSAR images are presented in Figure 11, where the dark areas indicate the oil spills. To compare the simulated results with the UAVSAR data, transects related to oil-free (red lines in Figure 11) as well as oil-covered sea surface (white lines in Figure 11) are extracted from SAR images and compared with the SSA-2 predictions. In order to compare the simulated results with measured data, the UAVSAR data are processed as follows. Firstly, a $100 \times 3300$ matrix is obtained by extracting 100 rows of pixels along the red and white lines in Figure 11. Then, a $1 \times 3300$ array can be obtained by computing the mean value of each column. Finally, the mean values are calculated in each $1°$ incident angle range.
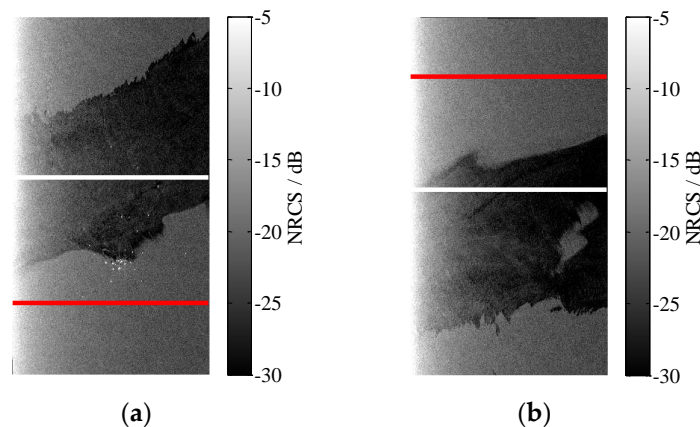


(a)  (b)

**Figure 11.** UAVSAR data. (**a**) Case (a). (**b**) Case (b).

Figure 12 presents the comparisons between the results simulated by the SSA-2 and UAVSAR data for sea surfaces without and with slicks, respectively. In Figure 12a, for slick-free sea surface, one can see that the VV-polarized NRCS simulated by the SSA-2 agrees well with the measured UAVSAR data. For HH polarization, the SSA-2 cannot provide a prediction as well as VV polarization. This conclusion is similar to the case of TSM presented by Wright et al. [36]. For the cross-polarized NRCS, the differences between the SSA-2 and UAVSAR are quite large. Additionally, there exist small differences between two UAVSAR images. This may be attributed to the differences of the thickness or the filling proportion between the two images. With respect to sea surface covered with slicks, the NRCSs of slick-covered sea surface with $F = 1$ and $F = 0.9$ are plotted in Figure 12b, 12c, and 12d, respectively. In Figure 12b, the fractional filling factor $F$ affects slick-b heavier than slick-a. The NRCS extracted from Case (a) agrees well with the results obtained based on slick-a for $F = 1$ and slick-b for $F = 0.9$. The NRCS extracted from Case (b) agrees well with the results obtained based on slick-a for $F = 0.9$. In fact, as the actual values of the physical parameters and the fractional filling factor for the oil spills in Figure 11 cannot be known, it is hard to compare the numerical results with measured data in detail.
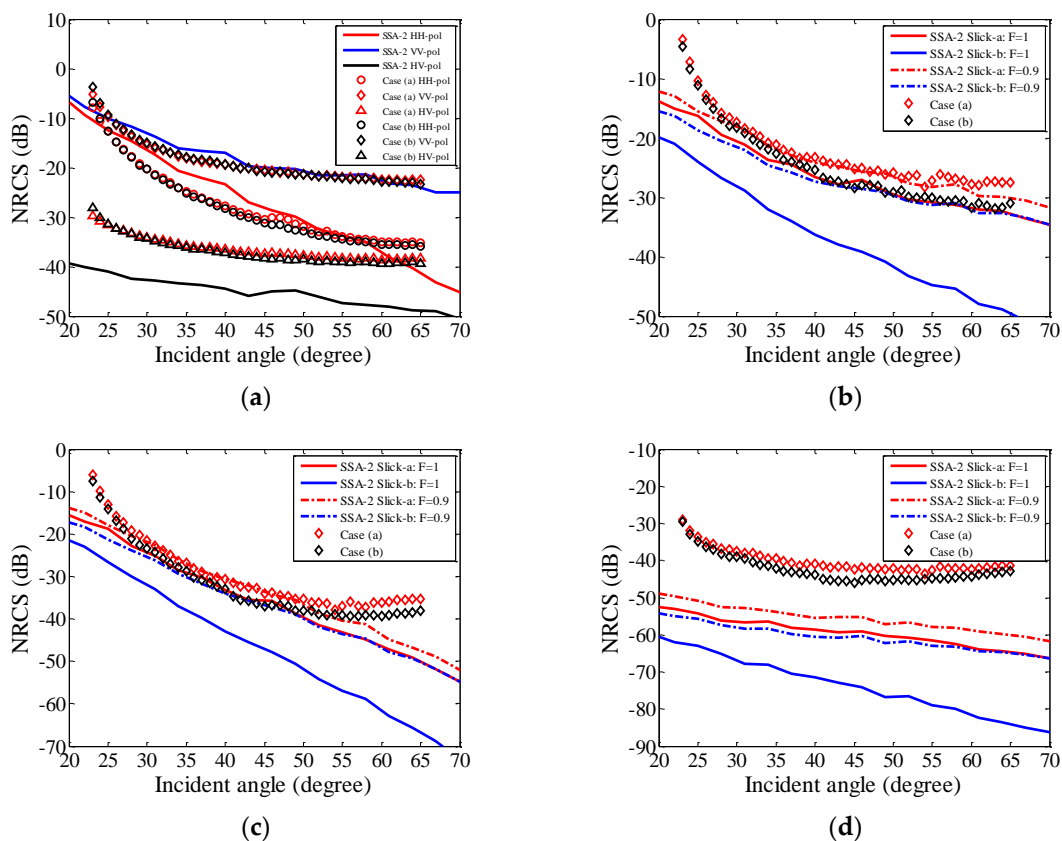
**Figure 12.** Comparison between the estimations of the SSA-2 and UAVSAR data. (**a**) Slick-free sea surface. (**b**) Slick-covered sea surface for VV polarization. (**c**) Slick-covered sea surface for HH polarization. (**d**) Slick-covered sea surface for HV polarization.

For HH-polarized NRCS, as exhibited in Figure 12c, the numerical results match well with the UAVSAR data for incident angles from 25° to 55°. In Figure 12d, there exist large differences between the simulated results and measured data for cross-polarized NRCS.

### 3.3. Distinguishing Ability of Different Bands

In previous sections, both for slick-free and slick-covered sea surfaces, it has shown that the SSA-2 could provide an accurate prediction for VV-polarized NRCS. In order to study the capacities of different bands for oil distinguish further, the slick-to-water contrasts at different bands are studied based on VV polarization. A slick-to-water contrast can be defined as [11]:

$$C = \left| \frac{\sigma_0^c - \sigma_0^f}{\sigma_0^c + \sigma_0^f} \right|, \tag{10}$$

where $\sigma_0^c$ is the NRCS of the slick-covered sea surface, and $\sigma_0^f$ is the NRCS of the slick-free sea surface. A larger value of *C* indicates that slick makes a more significant influence on NRCS. As a consequence, it can be more easily separated from sea backgrounds. Thus, the slick-to-water contrast can be taken as a measurement of distinguishability for different bands to separate slicks from sea backgrounds.

Figure 13 shows the slick-to-water contrasts evaluated with the SSA-2 as functions of incident angles. A common scatterometer typically operates at a moderate incident angle between about 20–60°. Thus, the incident angle is limited from 20° to 60°. Both for slick-a and slick-b, it seems that the value of C is larger for the smaller incident angle. The distinguishing abilities of four bands change with incident angle. For slick-a, it seems that the X-band has a larger C-value than other three bands for

incident angles smaller than about 35°. For incident angles between 35–60°, the C-band is preferred to distinguish slick-a. For slick-b, it seems that the C-band has a larger *C*-value than the other three bands for incident angles smaller than about 35°. For incident angles between 35–60°, the L-band performs better than the other three bands.
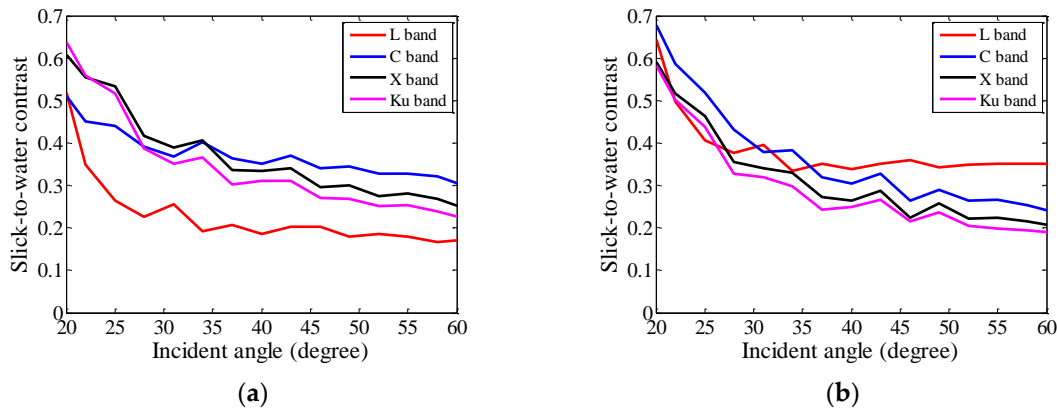


**Figure 13.** Slick-to-water contrast evaluated with the SSA-2 at different bands in relation to the incident angle, $U_{10}$ = 7 m/s. (**a**) Slick-a. (**b**) Slick-b.

## 4. Conclusions and Perspectives

In this paper, the EM backscattering from slick-free and slick-covered sea surfaces are investigated by the SSA-2 and measured SAR data. The slick-covered sea surface has been compared with the slick-free sea surface from several aspects, including the sea curvature spectrum, the RMS height, the RMS slope, and the autocorrelation function. According to the numerical simulations, we find that:

(1) The reduction of friction velocity mainly influences the large-scale waves and makes a slight influence on the small-scale waves. Meanwhile, the Marangoni effect mainly influences the small-scale waves.

(2) The influences of the Marangoni effect and *F* on the RMS height and the autocorrelation function are quite small. The reduction of friction velocity is the main reason for the changes of the RMS height and the autocorrelation function.

(3) By comparing the numerical results of the SSA-2 with GMFs, we can know that the SSA-2 provides accurate predictions for VV-polarized NRCS. Compared with the classic TSM, the SSA-1, the SSA-2 has more advantages in EM scattering simulations.

(4) By comparing the numerical results of the SSA-2 with measured SAR data, we can know that the SSA-2 provides accurate predictions for VV-polarized NRCS. The simulated VV polarized NRCS of the SSA-2 can be used to study the EM scattering from both slick-free and slick-covered sea surfaces.

(5) The distinguishing abilities (which are associated with the defined parameter 'slick-to-water contrast') of microwave scatterometers at various bands are different for different kinds of slicks and incident angles.

This work provides a basic study for EM scattering from slick-free and slick-covered sea surfaces. However, the comparisons between numerical simulations and measured data are only conducted at the C-band and L- band. In further works, more experiments and investigations will be carried out based on measured SAR data for other bands, especially the X-band and Ku-band.

**Author Contributions:** H.Z., Y.Z., and A.K. contributed the main idea. H.Z. performed the simulations and wrote the manuscript. H.G. contributed to the CMOD7 and modified the manuscript. Y.W. and C.Z. modified the manuscript.

## Appendix A

*Appendix A.1 Monte-Carlo Method for Sea Surface Profile Simulation*

The sea surface profile, which could provide some insights on the SAR imaging mechanism, is essential for the SSA-2 numerical simulation [37]. Assuming the side lengths of the simulated sea are $(L_x, L_y)$. The sampling numbers in $x$ and $y$ directions are $M$ and $N$. Therefore, $L_x = MdL_x$ and $L_y = NdL_y$, where $dL_x$ and $dL_y$ are the distances between two adjacent points in $x$ and $y$ directions. The sea surface height at $\mathbf{r} = (x, y)$ ($x = m_k \cdot dL_x$, $y = n_k \cdot dL_y$, where $m_k = -M/2 + 1, \ldots, M/2$, $n_k = -N/2 + 1, \ldots, N/2$) can be simulated with:

$$h(\mathbf{r}) = h(x, y) = \frac{1}{L_x L_y} \sum_{m=-M/2+1}^{M/2} \sum_{n=-N/2+1}^{N/2} T(k_m, k_n) \exp[i(k_m x + k_n y)], \tag{A1}$$

where

$$T(k_m, k_n) = 2\pi \left[ L_x L_y S(k_m, k_n) \right]^{1/2} \times \begin{cases} \frac{R(0,1)+iR(0,1)}{\sqrt{2}}, & m \neq 0, M/2 \text{ and } n \neq 0, N/2 \\ R(0,1), & m = 0, M/2 \text{ or } n = 0, N/2 \end{cases}. \tag{A2}$$
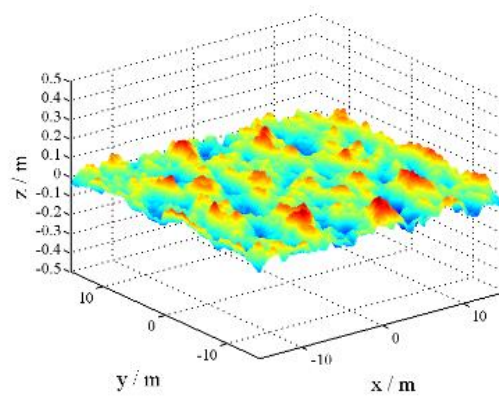
$S(k_x, k_y)$ is the two dimensions sea surface height spectrum. $k_x = m dk_x$ and $k_y = n dk_y$, where $dk_x = 2\pi/L_x$ and $dk_y = 2\pi/L_y$. $R(0, 1)$ is a Gaussian series with zero mean and unity standard deviation. To make the sea surface height $h(x, y)$ is real, $T(k_m, k_n)$ should satisfy $T(k_m, k_n) = T^*(-k_m, -k_n)$, $T(k_m, -k_n) = T^*(-k_m, k_n)$, where '*' denotes conjugate. In the numerical simulation, Equation (A2) is realized by using the inverse Fourier transform.

Figure A1 presents the generated two-dimension sea surfaces height without and with slicks. In this paper, there are 1024 sampling points at $x$ and $y$ directions, respectively. The sampling interval is $\lambda_i/8$, where $\lambda_i$ is the wavelength of the incident wave. In Figure A1, $\lambda_i$ is set as 0.2386 m which corresponds to L band. It can be easily seen that the large-scale waves of slick-covered sea surfaces are reduced due to the reduction of friction velocity.
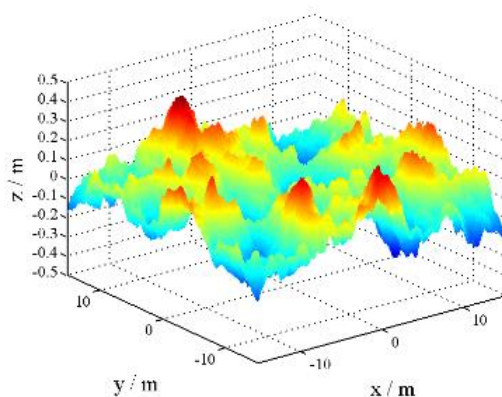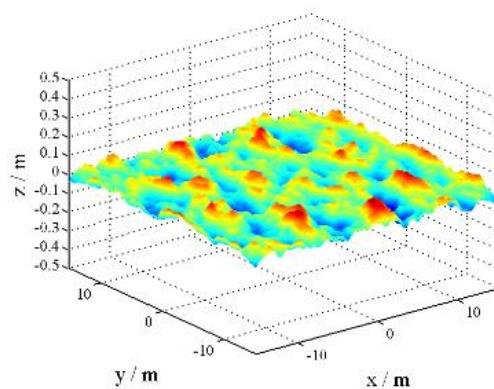


(**a**)

**Figure A1.** *Cont.*

(**b**)



(**c**)

**Figure A1.** Sea surface height, $U_{10}$ = 5 m/s. (**a**) Clean sea. (**b**) With slick-a. (**c**) With slick-b.

*Appendix A.2 The Second Order Small Slope Approximation*

The EM scattering configuration is plotted in Figure A2. Assuming the EM wave incidents on the two-dimension sea surface $z = h(\mathbf{r})$. The two-dimension sea surface height can be generated with the Monte-Carlo model. The incident wave vector denoted as $\mathbf{k}_i^e$ and the scattering wave vector denoted as $\mathbf{k}_s^e$. $\theta_i$, $\phi_i$, $\theta_s$, $\phi_s$ denote the incident angle, incident azimuth angle, scattering angle and scattering azimuth angle, respectively.
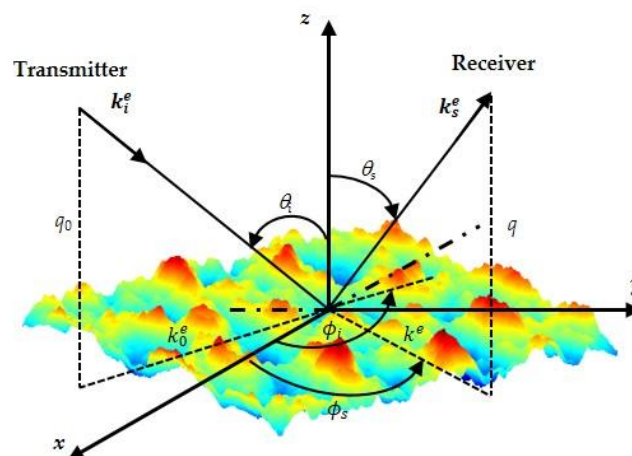


**Figure A2.** Configuration of EM scattering from sea surface.

The unit vector in the directions of incidence and scattering are:

$$\mathbf{k}_i^e = \mathbf{x} \sin \theta_i \cos \phi_i + \mathbf{y} \sin \theta_i \sin \phi_i - \mathbf{z} \cos \theta_i, \tag{A3}$$

$$\mathbf{k}_s^e = \mathbf{x} \sin \theta_s \cos \phi_s + \mathbf{y} \sin \theta_s \sin \phi_s - \mathbf{z} \cos \theta_s. \tag{A4}$$

$\mathbf{k}_i^e$ and $\mathbf{k}_s^e$ can be decomposed into horizontal and vertical components:

$$\mathbf{k}_0^e = k_i^e (\mathbf{x} \sin \theta_i \cos \phi_i + \mathbf{y} \sin \theta_i \sin \phi_i), q_0 = \sqrt{k^{e2} - k_i^{e2}}. \tag{A5}$$

$$\mathbf{k}^e = k_s^e (\mathbf{x} \sin \theta_s \cos \phi_s + \mathbf{y} \sin \theta_s \sin \phi_s), q = \sqrt{k^{e2} - k_s^{e2}}, \tag{A6}$$

where $k_i^e = |\mathbf{k}_i^e|$, $k_s^e = |\mathbf{k}_s^e|$, $k_0^e = |\mathbf{k}_0^e|$ and $k^e = |\mathbf{k}^e|$.

In the numerical simulations, the length of the simulated sea is finite, which leads to that the surface electric/magnetic current is forced to be zero at the boundary. If there is an abrupt change of surface electric/magnetic current from nonzero to zero, the effect of truncation would be very significant. To solve this problem, a tapered incident wave is used to make that the incident wave decays to zero in a Gaussian manner near the boundary [38].

The incident field can be written as:

$$\psi_{inc}(\mathbf{r}) = G(x, y, z) \exp(-i\mathbf{k}_i^e \cdot \mathbf{r}), \tag{A7}$$

where

$$G(x, y, z) = \exp[-ik_i^e(-x \sin \theta_i \cos \phi_i - y \sin \theta_i \sin \phi_i + z \cos \theta_i)\omega(x, y, z)] \exp(-t), \tag{A8}$$

wave $t = t_x + t_y$, and

$$t_x = \frac{(x \cos \theta_i \cos \phi_i + y \cos \theta_i \sin \phi_i + z \sin \theta_i)^2}{g^2 \cos^2 \theta_i}, t_y = \frac{(-x \sin \phi_i + y \cos \phi_i)^2}{g^2}, \tag{A9}$$

$$t = \frac{1}{k^2} \left[ \frac{(2t_x - 1)}{g^2 \cos^2 \theta_i} + \frac{(2t_y - 1)}{g^2} \right], \tag{A10}$$

$$\omega(x, y, z) = \frac{1}{k^2} \left[ \frac{(2t_x - 1)}{g^2 \cos^2 \theta_0} + \frac{(2t_y - 1)}{g^2} \right]. \tag{A11}$$

$g$ is the parameter that controls the tapering of the incident wave. In general, the value of g is between $L/4$ to $L/10$, depending on the incident angle. Here, $g$ is set as $L/6$. Moreover, it should be pointed out that, the taper function is not suited for problems of low grazing angle, i.e., $\theta_i \rightarrow 90°$.

The scattered field can be expressed as:

$$\psi_{sc}(\mathbf{r}) = q^{1/2} \int \exp[ik_s^e(x \sin \theta_i \cos \phi_i + y \sin \theta_i \sin \phi_i + z \cos \theta_i)] S(k^e, k_0^e) dk_s^e. \tag{A12}$$

In the case of far-field scattering, the scattering amplitude corresponding to the second-order SSA can be calculated with [19]:

$$\mathbf{S}(k^e, k_0^e) = \frac{2\sqrt{q_0 q}}{(q_0 + q)\sqrt{P_{inc}}} \int \frac{dr}{(2\pi)^2} G(r, h) \exp\left[-j(k^e - k_0^e) \cdot r + j(q_0 + q)h(r)\right]$$
$$\times \left[B(\mathbf{k}^e, \mathbf{k}_0^e) - \frac{j}{4} \int M(k^e, k_0^e; \xi) h(\xi) \exp(j\xi \cdot r) d\xi\right] \tag{A13}$$

where

$$M(k^e, k_0^e; \xi) = B_2(\mathbf{k}^e, \mathbf{k}_0^e; \mathbf{k}^e - \xi) + B_2(\mathbf{k}^e, \mathbf{k}_0^e; \mathbf{k}^e + \xi) + 2(q_0 + q)B_2(\mathbf{k}^e, \mathbf{k}_0^e). \tag{A14}$$

$B$ and $B_2$ are kernel functions which have been given in [19,20]. $h(\xi)$ is the Fourier transform of the sea surface height.

$P_{inc}$ is the incident wave power illuminated on the rough surface and can be expressed as:

$$P_{inc} = \int \int |\psi_{inc}(x,y,0)|^2 dxdy. \tag{A15}$$

The scattering coefficient can be calculated with scattering amplitude by:

$$\sigma_0 = 16\pi^3 q_0 q \Delta \mathbf{S}(\mathbf{k}^e, \mathbf{k}_0^e)[\Delta \mathbf{S}(\mathbf{k}^e, \mathbf{k}_0^e)]^*, \tag{A16}$$

where

$$\Delta \mathbf{S}(\mathbf{k}^e, \mathbf{k}_0^e) = \mathbf{S}(\mathbf{k}^e, \mathbf{k}_0^e) - \langle \mathbf{S}(\mathbf{k}^e, \mathbf{k}_0^e) \rangle. \tag{A17}$$

$\langle \cdot \rangle$ denotes the ensemble average operator. In this work, each NRCS is obtained over 80 realizations of sea surfaces. Limited by the length of the paper, parts of derivations of the SSA-2 are omitted here. For more details about the SSA-2, please see ref. [19,20].

**References**

1. Salberg, A.B.; Rudjord, Ø.; Solberg, A.H.S. Oil spill detection in hybrid-polarimetric SAR images. *IEEE Trans. Geosci. Remote Sens.* **2014**, *52*, 6521–6533. [CrossRef]
2. Skrunes, S.; Brekke, C.; Eltoft, T.; Kudryavtsev, V. Comparing Near-Coincident C- and X-Band SAR Acquisitions of Marine Oil Spills. *IEEE Trans. Geosci. Remote Sens.* **2015**, *53*, 1958–1975. [CrossRef]
3. Lupidi, A.; Staglianò, D.; Martorella, M.; Berizzi, F. Fast detection of oil spills and ships using SAR images. *Remote Sens.* **2017**, *9*, 230. [CrossRef]
4. Gleason, S.; Ruf, C.S.; Clarizia, M.P.; O'Brien, A.J. Calibration and Unwrapping of the Normalized Scattering Cross Section for the Cyclone Global Navigation Satellite System. *IEEE Trans. Geosci. Remote Sens.* **2016**, *54*, 2495–2509. [CrossRef]
5. Migliaccio, M.; Nunziata, F.; Buono, A. SAR polarimetry for sea oil slick observation. *Int. J. Remote Sens.* **2015**, *36*, 3243–3273. [CrossRef]
6. Solberg, A.H.S.; Brekke, C.; Ove Husoy, P. Oil spill detection in Radarsat and Envisat SAR images. *IEEE Trans. Geosci. Remote Sens.* **2007**, *45*, 746–755. [CrossRef]
7. Buono, A.; Nunziata, F.; Migliaccio, M.; Li, X. Polarimetric analysis of compact-polarimetry SAR architectures for sea oil slick observation. *IEEE Trans. Geosci. Remote Sens.* **2016**, *54*, 5862–5874. [CrossRef]
8. Migliaccio, M.; Nunziata, F.; Gambardella, A. On the co-polarized phase difference for oil spill observation. *Int. J. Remote Sens.* **2009**, *30*, 1587–1602. [CrossRef]
9. Migliaccio, M.; Gambardella, A.; Nunziata, F.; Shimada, M.; Isoguchi, O. The PALSAR polarimetric mode for sea oil slick observation. *IEEE Trans. Geosci. Remote Sens.* **2009**, *47*, 4032–4041. [CrossRef]
10. Migliaccio, M.; Nunziata, F. On the exploitation of polarimetric SAR data to map damping properties of the Deepwater Horizon oil spill. *Int. J. Remote Sens.* **2014**, *35*, 3499–3519. [CrossRef]
11. Zheng, H.; Zhang, Y.; Wang, Y.; Zhang, X.; Meng, J. The polarimetric features of oil spills in full polarimetric synthetic aperture radar images. *Acta Oceanol. Sin.* **2017**, *36*, 105–114. [CrossRef]
12. Ghanmi, H.; Khenchaf, A.; Comblet, F. Bistatic electromagnetic scattering and detection of pollutant on a sea surface. *J. Appl. Remote Sens.* **2015**, *9*, 096007. [CrossRef]
13. Pinel, N.; Déchamps, N.; Bourlier, C. Modeling of the bistatic electromagnetic scattering from sea surfaces covered in oil for microwave applications. *IEEE Trans. Geosci. Remote Sens.* **2008**, *46*, 385–392. [CrossRef]
14. Ghanmi, H.; Khenchaf, A.; Comblet, F. Numerical Modeling of Electromagnetic Scattering from Sea Surface Covered by Oil. *J. Electromagn. Anal. Appl.* **2014**, *6*, 15–24. [CrossRef]
15. Nunziata, F.; Sobieski, P.; Migliaccio, M. The two-scale BPM scattering model for sea biogenic slicks contrast. *IEEE Trans. Geosci. Remote Sens.* **2009**, *47*, 1949–1956. [CrossRef]
16. Alpers, W.; Hühnerfuss, H. The damping of ocean waves by surface films: A new look at an old problem. *J. Geophys. Res. Oceans* **1989**, *94*, 6251–6265. [CrossRef]

17. Rice, S.O. Reflection of electromagnetic waves from slightly rough surfaces. *Commun. Pure Appl. Math.* **1951**, *4*, 351–378. [CrossRef]

18. Ogilvy, J.A.; Merklinger, H.M. Theory of wave scattering from random rough surfaces. *J. Acoust. Soc. Am.* **1991**, *90*, 3382. [CrossRef]

19. Voronovich, A. Small-slope approximation for electromagnetic wave scattering at a rough interface of two dielectric half-spaces. *Wave Random Media* **1994**, *4*, 337–367. [CrossRef]

20. Voronovich, A.; Zavorotny, V. Theoretical model for scattering of radar signals in K u-and C-bands from a rough sea surface with breaking waves. *Wave Random Media* **2001**, *11*, 247–269. [CrossRef]

21. Kim, D.-J.; Moon, W.M.; Kim, Y.-S. Application of TerraSAR-X data for emergent oil-spill monitoring. *IEEE Trans. Geosci. Remote Sens.* **2010**, *48*, 852–863. [CrossRef]

22. Montuori, A.; Nunziata, F.; Migliaccio, M.; Sobieski, P. X-band two-scale sea surface scattering model to predict the contrast due to an oil slick. *IEEE J. Sel. Top. Appl. Earth Obs. Remote Sens.* **2016**, *9*, 4970–4978. [CrossRef]

23. Gade, M.; Alpers, W.; Hühnerfuss, H.; Wismann, V.R.; Lange, P.A. On the reduction of the radar backscatter by oceanic surface films: Scatterometer measurements and their theoretical interpretation. *Remote Sens. Environ.* **1998**, *66*, 52–70. [CrossRef]

24. Elfouhaily, T.; Chapron, B.; Katsaros, K.; Vandemark, D. A unified directional spectrum for long and short wind-driven waves. *J. Geophys. Res. Oceans* **1997**, *102*, 15781–15796. [CrossRef]

25. Zheng, H.; Khenchaf, A.; Wang, Y.; Ghanmi, H.; Zhang, Y.; Zhao, C. Sea Surface Monostatic and Bistatic EM Scattering Using SSA-1 and UAVSAR Data: Numerical Evaluation and Comparison Using Different Sea Spectra. *Remote Sens.* **2018**, *10*, 1084. [CrossRef]

26. Isoguchi, O.; Shimada, M. An L-band ocean geophysical model function derived from PALSAR. *IEEE Trans. Geosci. Remote Sens.* **2009**, *47*, 1925–1936. [CrossRef]

27. Stoffelen, A.; Verspeek, J.A.; Vogelzang, J.; Verhoef, A. The CMOD7 geophysical model function for ASCAT and ERS wind retrievals. *IEEE J. Sel. Top. Appl. Earth Obs. Remote Sens.* **2017**, *10*, 2123–2134. [CrossRef]

28. Mouche, A.; Chapron, B. Global C-Band Envisat, RADARSAT-2 and Sentinel-1 SAR measurements in copolarization and cross-polarization. *J. Geophys. Res. Oceans* **2015**, *120*, 7195–7207. [CrossRef]

29. Li, X.-M.; Lehner, S. Algorithm for sea surface wind retrieval from TerraSAR-X and TanDEM-X data. *IEEE Trans. Geosci. Remote Sens.* **2014**, *52*, 2928–2939. [CrossRef]

30. Wentz, F.J.; Smith, D.K. A model function for the ocean-normalized radar cross section at 14 GHz derived from NSCAT observations. *J. Geophys. Res. Oceans* **1999**, *104*, 11499–11514. [CrossRef]

31. Zhang, B.; Perrie, W.; Li, X.; Pichel, W.G. Mapping sea surface oil slicks using RADARSAT-2 quad-polarization SAR image. *Geophys. Res. Lett.* **2011**, *38*, L10602–L10606. [CrossRef]

32. Skrunes, S.; Brekke, C.; Eltoft, T. Characterization of marine surface slicks by Radarsat-2 multipolarization features. *IEEE Trans. Geosci. Remote Sens.* **2014**, *52*, 5302–5319. [CrossRef]

33. Li, H.; Perrie, W.; He, Y.; Wu, J.; Luo, X. Analysis of the polarimetric SAR scattering properties of oil-covered waters. *IEEE J. Sel. Top. Appl. Earth Obs. Remote Sens.* **2015**, *8*, 3751–3759. [CrossRef]

34. Liu, P.; Li, X.; Qu, J.J.; Wang, W.; Zhao, C.; Pichel, W. Oil spill detection with fully polarimetric UAVSAR data. *Mar. Pollut. Bull.* **2011**, *62*, 2611–2618. [CrossRef] [PubMed]

35. Carratelli, E.P.; Dentale, F.; Reale, F. On the effects of wave-induced drift and dispersion in the Deepwater Horizon oil spill. Monitoring and Modeling the Deepwater Horizon Oil Spill: A Record-Breaking Enterprise. *Geophys. Monogr. Ser.* **2011**, *195*, 197–204. [CrossRef]

36. Wright, J. A new model for sea clutter. *IEEE Trans. Antennas Propag.* **1968**, *16*, 217–223. [CrossRef]

37. Carratelli, E.P.; Dentale, F.; Reale, F. Numerical pseudo-random simulation of SAR sea and wind response. In Proceedings of the SEASAR, Frascati, Italy, 23–26 January 2006; pp. 1–5.

38. Tsang, L.; Kong, J.A.; Ding, K.-H.; Ao, C.O. Chapter 4 Random rough surface simulations. In *Scattering of Electromagnetic Waves: Numerical Simulations*; John Wiley & Sons: Hoboken, NJ, USA, 2004; pp. 111–176. ISBN 0-471-38800-9.